Stiffness Constants Prediction of Nanocomposites Using a Periodic 3D-FEM Model

Gabriele Cricrì,[1,2] Emilia Garofalo,[1] Francesco Naddeo,[1] Loredana Incarnato[1,2]

[1]Department of Industrial Engineering, University of Salerno, Fisciano (SA) 84084, Italy

[2]Research Centre NANO_MATES, University of Salerno, Fisciano (SA) 84084, Italy

Correspondence to: E. Garofalo (E-mail: egarofal@unisa.it)

Received 21 August 2011; revised 26 October 2011; accepted 28 October 2011; published online 19 November 2011
DOI: 10.1002/polb.23001

ABSTRACT: Predictive models, which enable the prediction of nanocomposite properties from their morphologies and account for polymer orientation, could greatly assist the exploitation of this new class of materials in more diversified and demanding market fields. This article focuses on the prediction of effective elastic properties (Young's moduli) of polymer nanocomposite films (copolyamide-6/nanoclay) using 3D analytical (based on the Mori-Tanaka theory) and 3D finite element (FE) models. The analytical model accounts for the orientation of polymer chains induced by drawing. 3D FE model exploits the representative volume element concept and accounts for the nanocomposite morphology as determined from transmission electron microscopy experiments. Model predictions were compared with experimental results obtained for nanocomposite films produced by means a pilot-scale film blowing equipment and collected at different draw ratios. © 2011 Wiley Periodicals, Inc. J Polym Sci Part B: Polym Phys 50: 207–220, 2012

KEYWORDS: finite element analysis; mechanical properties; nano-structures; nanocomposites; thin films

INTRODUCTION Polymer nanocomposites represent a promising new class of materials that contains inorganic particles-filled polymers for which at least one-dimension of dispersed particles is in the nanometer range. The fundamental length scales dominate the morphology and properties of these composites and the uniform dispersion of nanoscopically sized particles can lead to a very large interfacial area in which the distance between the nanoelements begins to approach molecular dimensions. The intimate interactions between the organic and inorganic phases create bulk materials dominated by solid-state physics on the nanoscale, with synergistic properties possible. Polymer nanocomposites offer the possibility of developing new materials with their own range of structure-property relationships, only indirectly related to their components and their micron- and macroscale composite counterparts. This aspect, coupled with the ability to process such materials with conventional plastic processing equipment, would lead to a net improved performance/cost over the design of new polymers or multilayer materials.[1–7] In particular, great industrial and scientific attention is paid toward layer-shaped nanofillers, sheets from only one to few nanometers thick and hundreds or thousands nanometers wide and long. These materials show high aspect ratios and have exceptionally high stiffness compared with most polymers and even many other kinds of fillers. Such properties enable the clay layers, when dispersed in a polymer matrix, to carry a significant component of the applied load, considerably improving the tensile mechanical properties of the neat matrix.[8–10] Moreover, because of the very large surface areas and the small interparticle distances, the platelets can, in principle, significantly modify the properties of the polymer matrix, like polymer crystalline morphology, chain conformation, and dynamics through so-called "confinement effects."[11–14]

Investigation of the relationship between processing, morphology, and properties of the nanocomposite systems by means of theoretical, analytical, and/or numerical tools is an alternative and complementary route to the experimental approach. It enables to take into account the effects of different morphology descriptors (the silicate interlayer spacing, the average number of clay layers per stack, the interlayer gallery material, etc.), which cannot be directly accessed experimentally or at least their measurement can be quite cumbersome. Several attempts to model the effects of geometrical and material parameters on the elastic behavior of polymer-clay nanocomposites have been already reported,[15–30] and it is important to emphasize that numerous complexities arise when comparing composite theory to experimental data. First of all, the ideal situation of full exfoliation, dispersion, and orientation, supposed by several models, is not usually achieved. In the commonly occurring case, the distribution of the clay particles aspect ratio is wide, and the silicate platelets are not fully dispersed and oriented. Thus, the accuracy of the mechanical modeling of the nanocomposites is crucially

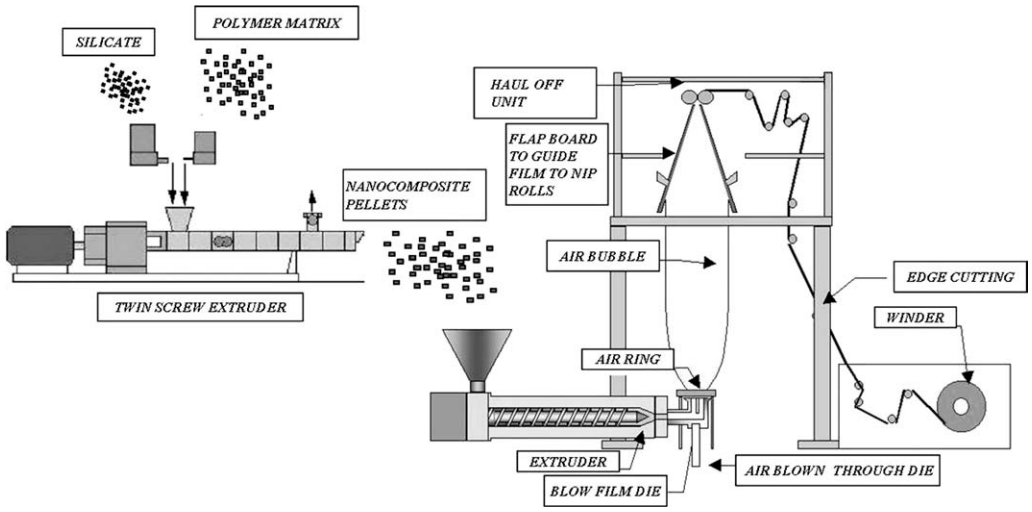

FIGURE 1 Scheme of processing for the production of HADS nanocomposite films.

dependent on the properties of the "effective particle." Concepts such as "matrix" and "particle," which are well-defined in conventional two-phase composites, can no longer be directly applied to polymer-clay nanocomposites due to the hierarchical nanometer length-scale morphology of the particle structure and surrounding matrix.[24–26,31–34] The more recent hierarchical modeling techniques take into account not only the influence of the interphase around nanoinclusions but also the effect of the size and shape (geometry and waviness) of the nanoparticles on the stiffness and viscoelastic response of polymer nanocomposites.[31–34] Most of the micromechanical models (numerical as well as analytical), reported in literature for polymer layered-silicate nanocomposites, were used to predict the tensile mechanical behavior of injection molded nanocomposites[15,25,29] or hybrid systems characterized by a well-defined stratified nanostructure.[31,32] On the other hand, modeling techniques, which enable the prediction of nanocomposite film properties from their nanostructure and account for polymer and platelets orientation, due to the film extrusion operations, are highly demanded by the industry, because a better understanding of the influence of processing conditions on nanocomposite film performances represents a key issue to facilitate the design and development of these systems for packaging applications.

This manuscript, incorporating the combination of experiments, numerical computations, and theory, focuses on the modeling of mechanical behavior of polyamide based nanocomposites, produced by means a pilot-scale film blowing equipment and collected at different draw ratios. At this purpose, a three-dimensional finite element model has been realized by means of an original algorithm that generates the clay particles position taking into account the different density of distribution along the three main processing directions of the film and the measured orientations of nanoclays. Furthermore, the matrix is considered to be elastically orthotropic to properly account the effect of the biaxial drawing on the polymer stiffness. Moreover, periodic boundary conditions and an original representative volume element (RVE) sizing method were used to minimize the dimensions of the RVE that gives acceptable scatter. In this way, the mean values of the elastic modules, for even RVEs containing very few particles, are close to the exact values for large composite volume and overlong computational times are avoided. Experimental elastic constants of the polyamide nanocomposite films were also compared with analytical predictions based on the Mori-Tanaka approach that was properly modified to take into account the mechanical orthotropic characteristics of the polymer matrix upon drawing.

EXPERIMENTAL

In this section of this article, brief description of the materials and techniques, used to prepare and characterize the nanocomposite films, has been reported. Moreover, an accurate and semi-automatic image analysis, for all the nanocomposite samples, has been performed to evaluate the morphological parameters to be used as input variables in the analytical and numerical models.

Film Preparation

A copolyamide of nylon-6 (denoted HADS and supplied by Caffaro SpA) was used as polymer matrix. The copolyamide investigated has been obtained by random polymerization of ε-caprolactam in the presence of the comonomer 1, 1",3-trimethylcyclohexyl-3-methylamine-5-isophthalamide at 5 wt %. The silicate used in the preparation of the hybrids was Cloisite 30B (supplied by Southern Clay Products), a layered sodium montmorillonite organically modified by methyl, tallow, bis-2-hydroxyethyl quaternary ammonium chloride (90 meq/100 g clay), having an interlayer basal spacing $d_{001} = 18.5$ Å. Nanocomposites pellets were initially prepared by melt compounding and then used as feed for the following film blowing extrusion, as schematized in Figure 1.

The melt compounding, fundamental to achieve satisfactory degree of silicate exfoliation, was realized using a twin-screw extruder having counter-rotating intermeshing cone-shaped screws with $L = 500$ mm and, at the end of the extruder, a

TABLE 1 Sample Nomenclature of Neat copolyamide and Nanocomposite Films at Blow Up Ratio = 2.5 and Stretched at Two Different Draw Ratios (DR = 23 and DR = 35)

	Nominal wt % Cloisite 30B		
Draw ratio	0	3	6
23	HADS23	3HADS23	6HADS23
35	HADS35	3HADS35	6HADS35

circular die with a diameter $D = 2.5$ mm. A temperature profile of 250–245–245–245 °C from hopper to die was imposed and a screw speed of 100 rpm was set. Before processing, the materials were dried in a vacuum oven at 90 °C for 18 h, resulting in a moisture level of less than 0.2 wt %, to avoid polymer degradation during processing.

The effective level of organoclay into each extruded sample was determined by thermogravimetric analysis, which was carried out with a TGAQ500 (TA Instruments), from 25 to 900 °C at a thermal scan rate of 10 °C/min in air atmosphere. The amount of residue was corrected for the loss of organic component present in Cloisite 30B. Each determination was replaced on five specimens to obtain statistical silicate loading values.

Blown films were prepared using a Brabender DCE 330 single-screw extruder ($L = 400$ mm and $L/D = 20$), equipped with an annular die (30 and 32 mm inner and outer diameters, respectively). A temperature profile of 242–245–245 °C from hopper to die was imposed, and a screw speed of 15 rpm was set. The films were collected with blow up ratio equal to 2.5 and two different stretching ratios (DR = 23 and DR = 35). The nomenclature used to identify the different films is reported in Table 1, and it is based on three indexes indicating the Cloisite 30B loading, the polymer matrix, and the draw ratio applied, respectively.

Film Characterization

Nanomorphology

Transmission electron microscopy (TEM) represents until now the more appropriate technique to investigate the orientation and the dispersion of nanoclay in polymer silicate nanocomposites. TEM analysis was conducted using a Philips EM 208 with different magnification levels. The images were captured both on sections parallel and perpendicular to the extrusion direction, which were prepared by microtoming of ultra-thin specimens with a Leica Utracut UCT microtome.

The determination of filler aspect ratio for layered aluminosilicate hybrids is not straightforward, because various complications arise from intrinsic variations in both length and thickness of the silicate platelets. The recovery, refinement, and chemical treatment of clays may contribute to the variation in filler geometry. Furthermore, extrusion of the silicate with polymer and any additional melt processing steps, as injection molding, film extrusion, and so on, will amplify the range of particle shapes and sizes, particularly when the organoclay is not completely exfoliated.

TEM images of 6 wt % nanocomposite blown films are reported in Figure 2(a,b). Both the films were characterized by a mixed intercalated-exfoliated nanostructure with a satisfactory dispersion of the silicate on nanometric scale. However, a more uniform distribution of the clay platelets was observed for the nanocomposite films obtained at DR = 23, whereas the more stretched sample displayed bigger stack of silicate layers. A recent study,[35] carried out by our research group on nanostructural arrangements induced by uniaxial drawing, has demonstrated that the application of high draw ratios, particularly in the case of the more loaded hybrids, can induce silicate aggregation as a consequence of the combination of reduced cross area section upon stretching and face-to-face electrostatic interactions between adjacent silicate platelets.

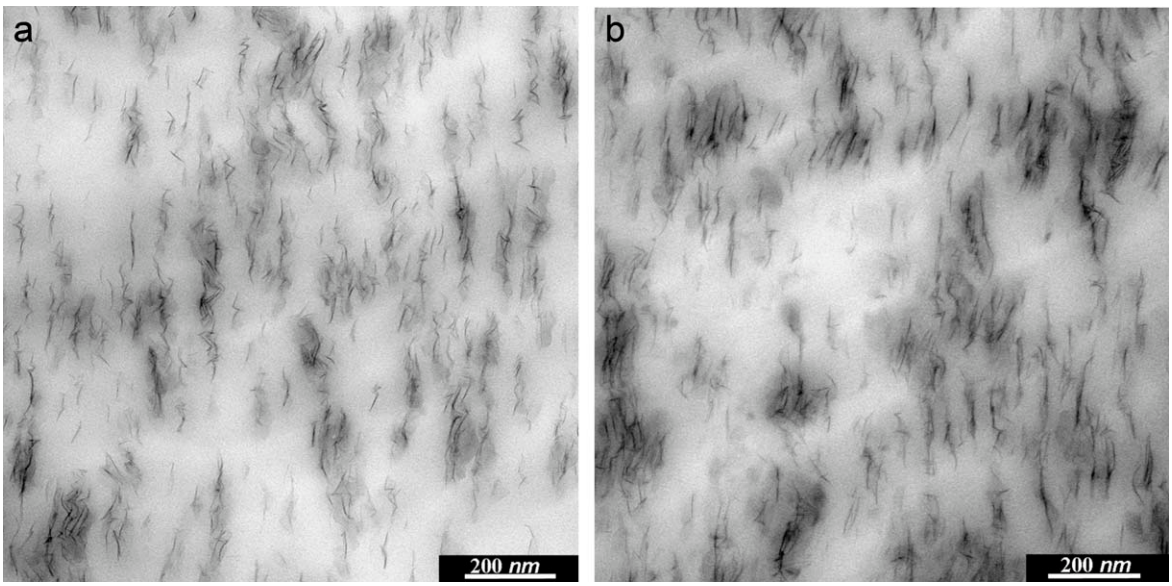

FIGURE 2 TEM images of 6% HADS films sectioned orthogonally to the extrusion direction: (a) DR = 23; (b) DR = 35.

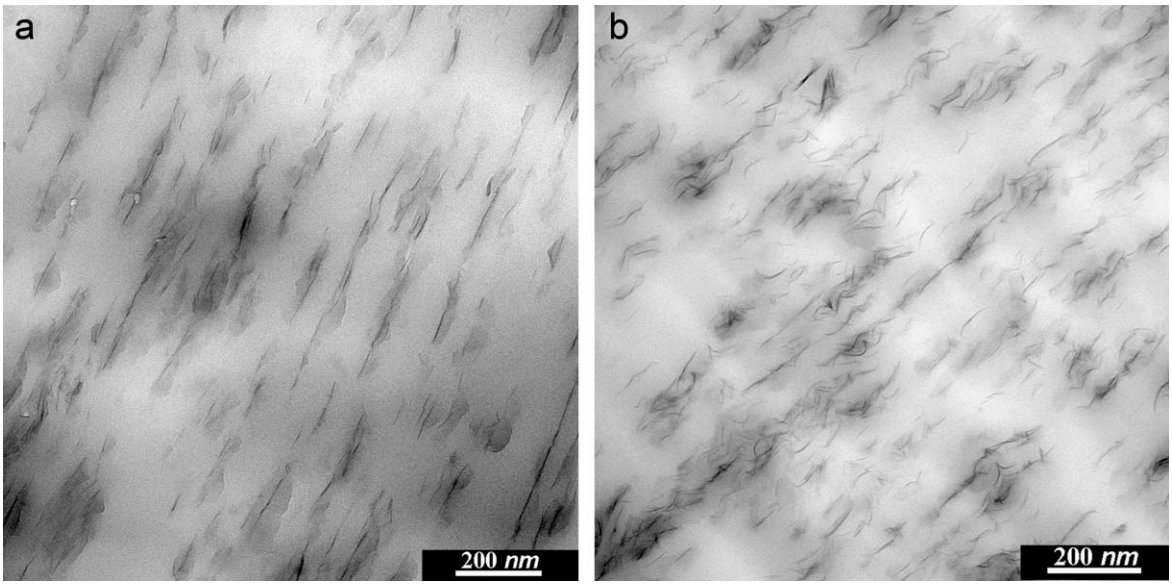

FIGURE 3 TEM images of 3 wt % nanocomposite film at DR = 23, sectioned (a) along the draw direction (MD) and (b) perpendicular to the draw direction (TD).

To study the orientation distribution of the clay particles in the hybrid films, TEM analysis was also carried out on sections both parallel and normal to the film extrusion direction. In Figure 3, the micrographs of 3 wt % nanocomposite film at DR = 23, sectioned along the draw direction (MD) and perpendicular to the stretching direction (TD), are reported.

The combination of these two images indicates that the clay layers are mainly oriented parallel to the film plane and that they slightly buckle perpendicularly to the draw direction. Compressive strain in this direction arises from the Poisson effect, which results in decreased film thickness with increasing the deformation along the stretching direction.[36]

An accurate and semi-automatic image analysis was performed for all the nanocomposite samples to evaluate the geometrical (average diameter, $<D>$) and spatial characteristics (θ_x and θ_z distributions) of the exfoliated silicate platelets, schematically represented as cylindrical particles with height of 1 nm (Fig. 4). Moreover, for this analysis, the stacking of platelets within a cluster was treated in a simplified way, as shown in Figure 4.

Most image analysis tools are not able to accurately discriminate between grayish polymeric regions and the dark lines corresponding to aluminosilicate platelets. Thus, using commercial image analysis software, TEM micrographs of the blown films were previously converted into black and white images, by applying a threshold value properly chosen to not modify the original filler nanostructure. Then, the morphological parameters of the hybrid films were evaluated by following the method proposed by Vermogen et al.[37] Images were taken at different magnifications to include in the analysis different types of clay platelets (individual sheets, thinner tactoids, thicker tactoids, and agglomerates) to provide a good statistics of the distribution of the filler in the matrix. The number of platelets in a tactoid was calculated using the formula $N = (t_{\text{particle}} + d_{001} - t_{\text{platelet}})/d_{001}$, where N is the number of platelets per particle, t_{particle} is the thickness of the particle measured by TEM, d_{001} is the d-spacing also

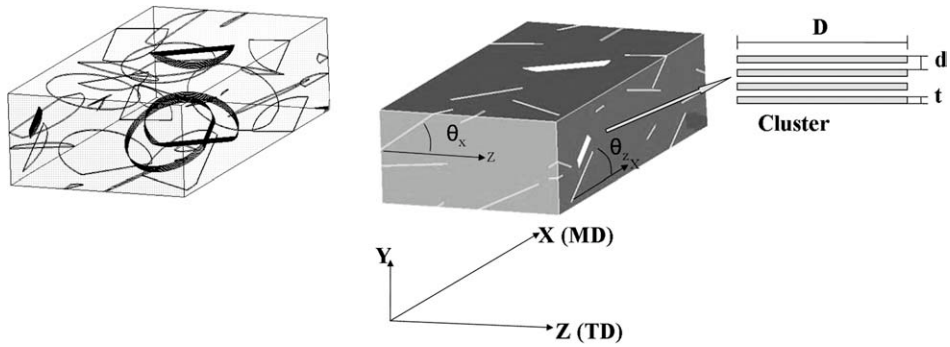

FIGURE 4 Schematic view of geometric (D) and spatial parameters (θ_x,θ_z) of the exfoliated silicate platelets and intercalated clusters in the nanocomposite films.

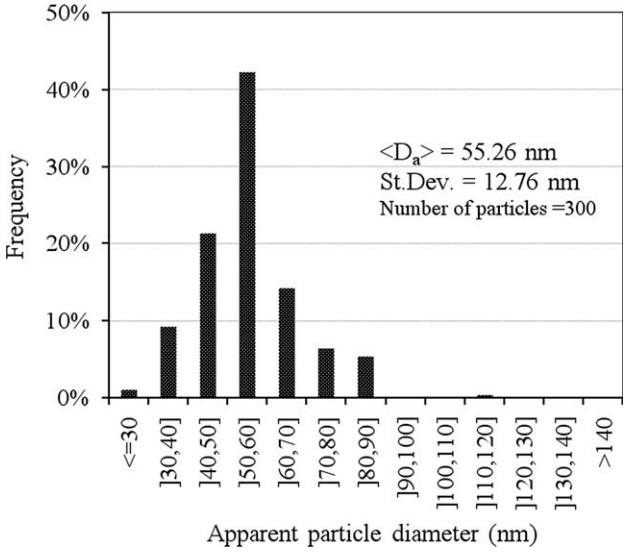

FIGURE 5 Histogram of MMT particle diameter.

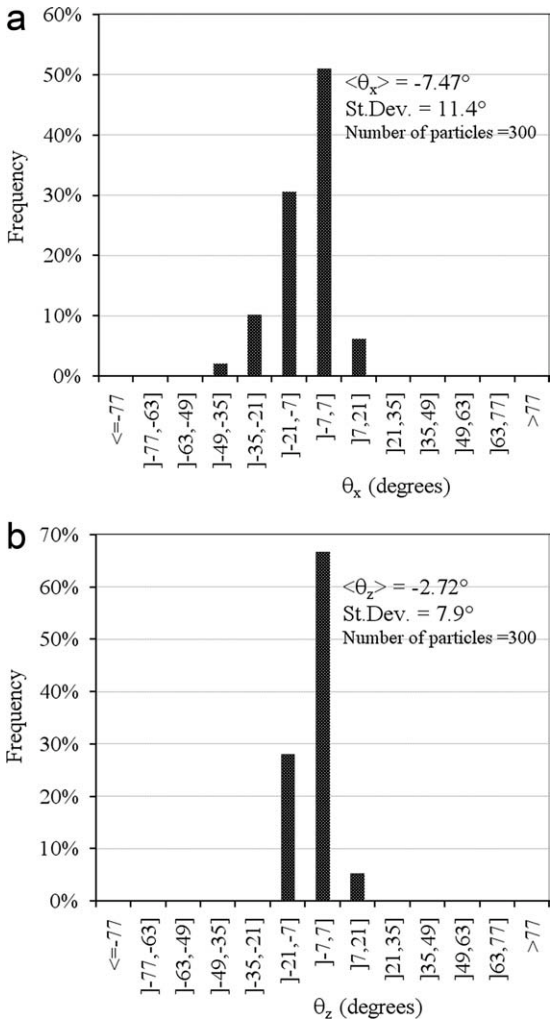

FIGURE 6 Histograms of MMT particles spatial distributions for 3HADS23 blown film: (a) θ_x distribution and (b) θ_z distribution.

measured by TEM, and $t_{platelet}$ is the estimated[15] thickness of a single platelet (ca. 1 nm). Around 300 tactoids/platelets were considered for each measurement.

In Figure 5, frequency histogram of MMT apparent particle diameter ($<D_a>$) is shown and pertinent statistical data, obtained analyzing a consistent number of nanocomposite TEM micrographs are reported. The experimental value $<D_a> = 55$ nm is smaller than the true diameter of the silicate platelets ($<D>$). In fact, microtoming of the hybrid samples into thin sections for TEM analysis results in an apparent distribution of the observed particle sizes even if all disk-like platelets were the same size. On the basis of such considerations, the true average particle diameter is then $<D> \approx 70$ nm, taking into account that $<D_a>$ represents the mean value of the chord of the circle having the same diameter of the disk-like platelet.

The spatial characteristics of the silicate particles in the polymer matrix were also determined. In Figure 6(a,b), the frequency histograms, reporting θ_x and θ_z distributions for 3HADS23 hybrid film, are shown. The clay platelets arranged themselves substantially parallel to 3HADS23 film surface, as well as in all the nanocomposite samples. However, the standard deviations of θ_x and θ_z for every blown film were introduced as input parameters both in numerical and analytical model, and their values are reported in Table 2.

Finally, the volumetric clay compositions and volume fraction of intercalated particles for the hybrid films were also determined. An average percentage of intercalated clusters were evaluated equal to 25% for each nanocomposite blown film and a *d*-spacing (*d*) of 2 nm was measured. Upon stretching, the number of clay layers per stack varied from 5 to 6 for the HADS films at 3 wt % of silicate content. In the more loaded samples, bigger stacks of filler were observed.

Mechanical Properties

Mechanical tests were carried out, according to ASTM standard D-638, by an Instron 4301. The films were tested with a grip distance of 40 mm and a cross-head speed of 5 mm/min to measure the Young's modulus both parallel (MD) and perpendicular (TD) to the extrusion direction. The stiffness data are reported in Table 3 for both neat HADS and nanocomposite blown films. At any draw ratio, the hybrid films showed better mechanical properties compared with the unfilled systems. In particular, the presence of the silicate leads to substantial improvements in stiffness, and this phenomenon is more pronounced in the case of blown films at DR = 35. Furthermore,

TABLE 2 θ_x and θ_z Standard Deviations for all the Tested Nanocomposite Films

	Standard Deviations (degrees)	
Sample	θ_x	θ_z
3HADS23	11.4	7.9
3HADS35	23.0	13.8
6HADS23	28.0	16.4
6HADS35	17.0	10.2

TABLE 3 Young's Modulus of Neat HADS Films and the Nanocomposite Films at Blow Up Ratio = 2.5 and Stretched at Two Different Draw Ratios (DR = 23 and DR = 35)

	Young's Modulus (MPa)			
	DR = 23		DR = 35	
Sample	E_x (MD)	E_z (TD)	E_x (MD)	E_z (TD)
HADS	1,200 ± 80	1,000 ± 70	600 ± 60	320 ± 70
+3%	1,950 ± 80	1,800 ± 80	1,300 ± 60	1,300 ± 80
+6%	1,900 ± 90	1,740 ± 80	1,600 ± 80	1,170 ± 70

the mechanical properties of the nanocomposites at higher silicate content (6 wt %) slightly decrease compared with 3 wt % hybrids. These results may be due to the higher presence of nanofiller that favors nanoparticle face-to-face interactions leading to the formation of silicate aggregates.[35]

With regard to the effect of drawing on film stiffness, the performance worsening, observed for samples obtained at higher DR, can be attributed not only to silicate reaggregation upon stretching but also to strain-induced crystalline phase changes to which polymer chains undergo during the process. More details are reported in our previous publications.[38,39]

To implement both the analytical and numerical model, linear orthotropic characteristics were taken into account for the polymer matrix (subscript m), according to the film processing conditions. In particular, a film can be reasonably considered as an orthotropic lamina. The simplest form of anisotropy in polymers, in fact, results when fibers or films are prepared by deforming them plastically using a stretching process know as drawing, and so they possess isotropy in planes perpendicular to the direction of drawing.[40,41] In the plane stress-state hypothesis (plane of the film), it was possible to calculate the shear modulus G_{mxz}, starting from the experimental values of E_{mx}, E_{mz}, E_{mk}, (where k is the direction forming a 45° angle with x and z directions) and assuming the Poisson ratio $\nu_{mxz} = 0.35$.[15]

Moreover, regarding to the films prepared in this work, the macromolecules are probably oriented along the prevalent stretching direction x. Then, it is reasonable to assume a comparable mechanical behavior of the polymer along the orthogonal directions y, z, that is:

$$E_{mz} = E_{my}; \quad G_{mxy} = \left(\frac{4}{E_{mk}} - \frac{1-2\nu_{mxy}}{E_{mx}} - \frac{1}{E_{my}}\right)^{-1} = G_{mzx}; \quad \nu_{mxy} = \nu_{mzx} \tag{1}$$

The conditions $G_{mxy} = G_{myz}$ and $\nu_{mxy} = \nu_{myz}$ were also imposed, because these assumptions do not significantly affect the reliability of simulations. In particular, a sensitivity analysis has been performed by means of the 3D-FEM model, showing that the neat polymer parameters (E_{my}, G_{mzx}, G_{myz}, ν_{mxy}, and ν_{myz}) variation does not significantly affect the experimental values of the composite stiffness constants (E_x, E_z). For brevity, the details have been omitted in this article.

The resulting shear modules ($G_{mxy} = G_{mzx} = G_{myz}$) of the unfilled films at DR = 23 and DR = 35 are equal to 323 MPa and 395 MPa, respectively. For silicate nanoparticles (subscript f), linear isotropic characteristics were, instead, considered ($E_f = 176$ GPa; $\nu_f = 0.25$).[27]

Finally, matrix properties are assumed to be homogeneous, even close to the particles. It is worthy to point out that some researchers retain that surfactant might play an important role in determining the nanocomposite mechanical behavior. However, experimental evidence relating to that issue is lacking, and hence, it is not able to properly account for the surfactant contribution either to the exterior platelet surfaces or to the galleries between clay layers.

ANALYTICAL MODEL

The Mori-Tanaka micromechanical model, due to its relative simplicity and usefulness, is widely used to evaluate the effective stiffness tensor in two-phase composite materials with ellipsoid-like inclusions. The model was thought to simulate similar and aligned inclusions, with dilute volume fractions. Nevertheless, many authors have extended the application of the model for taking into account also a generic spatial orientation distribution,[42] and even multishaped or multiphase nanocomposite systems. An original application of the Mori-Tanaka model was performed by Benveniste[43] for a two-phase composite material, which estimate of the effective stiffness was:

$$C^{\text{eff}} = C_1 + f_2\{(C_2 - C_1)T\}[f_1 I + f_2\{T\}]^{-1} \tag{2}$$

where the curly brackets indicate averaging over all possible directions, indices "1" and "2" denote the matrix and the inclusions phase, respectively, f_i is the ith phase volume fraction, I represents the fourth-order identity tensor, and T is defined by:

$$T = \left[I + SC_1^{-1}(C_2 - C_1)\right]^{-1} \tag{3}$$

where S is the Eshelby tensor.

It is well known[44] that, for composites with general random orientation, the averaging procedure defined in eq 3 gives stiffness tensors that can violate the major symmetry conditions. For this reason, the averaging method used here is applied to the whole stiffness tensor, to rigorously preserve $C_{ijkl} = C_{klij}$:[45]

$$C^{\text{eff}} = \left\{C_1 + f_2(C_2 - C_1)T[f_1 I + f_2 T]^{-1}\right\} = C_1 + f_2\{C^{\text{var}}\} \tag{4}$$

$$C^{\text{var}} = C^{\text{var}(x_0)} \cdot r \cdot r \cdot r \cdot r = \left[(C_2 - C_1)T[f_1 I + f_2 T]^{-1}\right]_{(x_0)} \cdot r \cdot r \cdot r \cdot r \tag{5}$$

or, in components:

$$C_{ijkl}^{\text{var}} = r_{ip} r_{jq} r_{kr} r_{ls} C_{pqrs}^{\text{var}(x_0)} \tag{6}$$

where (x_0) denotes the reference coordinate system and the rotation matrix r_{ij} is a function of the Euler angles (ψ,θ,φ) of the ellipsoid rotation.

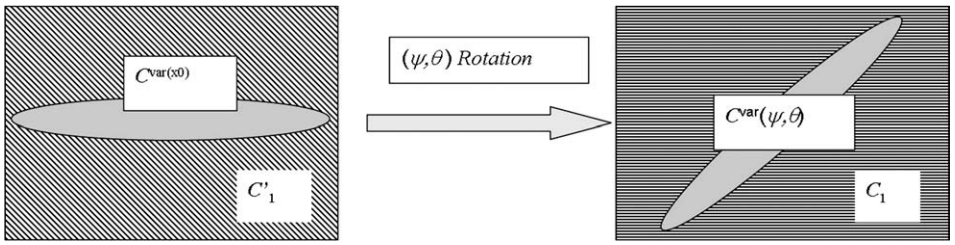

FIGURE 7 Rotation of the single (or aligned) inclusion model.

In this work, a simple spatial orientation distribution function is used, given in terms of the Euler angles (ψ,θ) of the normal to the plane containing the penny-shaped inclusions, capable to reproduce fully aligned particles distributions as well as totally random ones. This orientation function is, in particular, used to simulate a non uniform distribution along three orthogonal axes corresponding to the orthotropic axes of the nanocomposite film. Once fixed the orientation distribution $f(\psi,\theta)$, the average operation can be written as:

$$\{C^{\text{var}}\} = \iint_{D(\psi_{\max},\theta_{\max})} f(\psi,\theta) C^{\text{var}}(\psi,\theta) d\psi d\theta \tag{7}$$

The following orientation distribution was used:

$$f(\psi,\theta) = \begin{cases} a\big(1 + A_\psi \cos(2\psi)\big)(1 - A_\theta \sin\theta)\sin\theta & (\psi,\theta) \in D(\psi_{\max},\theta_{\max}) \\ 0 & (\psi,\theta) \in [0,\pi]\times[0,\pi] - D(\psi_{\max},\theta_{\max}) \end{cases} \tag{8}$$

where:

$$a = 1/\big(2\psi_{\max} + A_\psi \sin(2\psi_{\max})\big) \times [4(1-\cos\theta_{\max}) - A_\theta(2\theta_{\max} - \sin(2\theta_{\max}))] \tag{9}$$

$$D(\psi_{\max},\theta_{\max}) = ([0,\pi] -]\psi_{\max}, \pi - \psi_{\max}[) \times ([0,\pi] -]\theta_{\max}, \pi - \theta_{\max}[) \tag{10}$$

$$\psi_{\max} = \begin{cases} \frac{1}{2}\left(\pi - \cos^{-1}\frac{1}{A_\psi}\right) & A_\psi > 1 \\ \frac{\pi}{2} & A_\psi \le 1 \end{cases} \tag{11}$$

$$\theta_{\max} = \begin{cases} \sin^{-1}\left(\frac{1}{A_\theta}\right) & A_\theta > 1 \\ \frac{\pi}{2} & A_\theta \le 1 \end{cases} \tag{12}$$

The distribution parameters A_ψ and A_θ rule the variance of the Euler angles (ψ,θ), responsible for the orthotropic grade of the composite. If $A_\psi = A_\theta = 0$, the distribution is uniform, and the resulting effective stiffness tensor is isotropic. The angles θ_z and θ_x are related to the Euler angles by the following relation:

$$\begin{Bmatrix} \theta_z \\ \theta_x \end{Bmatrix} = \begin{Bmatrix} \tan^{-1}(\tan\theta\sin\psi) \\ \tan^{-1}(\tan\theta\sin\psi) \end{Bmatrix} \tag{13}$$

Then, it is possible to relate the distribution parameter A_ψ and A_θ to the variance $\text{Var}(\theta_z)$ and $\text{Var}(\theta_x)$ of the above angles that can be straightforward evaluated from the experimental tests.

In this work, the matrix phase of the nanocomposite C_1 has been considered orthotropic, with the orthotropic axes parallel to the draw direction (MD), normal to it (TD) in the film plane and normal to the film plane. For this reason, a general form of the Eshelby tensor $S^{(x_0)}$ needs to be used into eq 3; for brevity, such expression was not explicitly reported here and it can be found, for example, in Kinoshita and Mura.[46] Furthermore, the expression of the C^{var} tensor (eq 5) in the general (rotated) case has to be substituted in eq 7. It can be done by operating a rotation (ψ,θ) on the tensor $C^{\text{var}(x_0)}$. This latter depends both on the inclusion material and shape, and the backward rotated C_1 tensor, $C'_1 = C_1 \cdot r^T \cdot r^T \cdot r^T \cdot r^T$:

$$\begin{aligned} C^{\text{var}(x_0)} &= \big(C_2 - C'_1\big) T^{(x_0)} \Big[f_1 I + f_2 T^{(x_0)}\Big]^{-1}; \\ T^{(x_0)} &= \Big[I + S^{(x_0)} C'^{-1}_1 \big(C_2 - C'_1\big)\Big]^{-1} \end{aligned} \tag{14}$$

In Figure 7, the above cited backward–forward rotation is represented for clarity.

The evaluation of the effective stiffness C^{eff} requires two levels of numerical integration over spherical surfaces: the first, necessary for the general Eshelby tensor $S^{(x_0)}$ calculation, has been performed by using 20,000 integration points in the interval $[0,2\pi] \times [0,\pi]$; the second, used to calculate the expression in eq 7, has been found to need only 9 Gauss points in the interval $[0,\psi_{\max}] \times [0,\theta_{\max}]$. Moreover, this latter takes into account the double symmetry due to the ortotropy of the effective stiffness.

In the framework of the present Orthotropic Mori-Tanaka (OMT) model, the aspect ratio of the MMT particles was estimated for each hybrid sample, taking into account both the exfoliated platelets and the intercalated stacks. In Table 4,

TABLE 4 Orthotropic Mori-Tanaka Model Parameters

Sample	Aspect Ratio	A_ψ	A_θ
3HADS23	56.0	0.75	2.1
3HADS35	55.5	1.05	1.14
6HADS23	55.5	0.98	1.27
6HADS35	53.8	0.85	1.57

the aspect ratio values and parameters A_ψ and A_θ related to the θ_x and θ_z standard deviations are reported.

NUMERICAL MODEL

A three-dimensional finite element model was realized using an original algorithm that generates the clay particles position to take into account the real geometrical characteristics of the nanocomposites produced by the film blowing technique.

The aim of this section is to create an easily manageable parametric FEM model, which has all the information concerning with the morphology of the hybrids and the mechanical properties of the composite phases. Moreover, the nanocomposite systems were represented by a periodic distribution of the particles in an infinite matrix. The repetitive cell of this distribution is a reasonably small portion of space (RVE) of brick form (Fig. 8), to minimize FEM runs' computational times.

Particle Random Generation

The algorithm, used to implement the 3D numerical model reported in this article, consists of two routines running in different programming environments that are Matlab and Ansys.

In this model, the nanoparticles of approximately ellipsoidal shape were modeled as disks (Fig. 8), whose geometric parameters' values were mediated from those extrapolated by TEM image analysis.

The portion of algorithm written in Matlab randomly generates the platelets location and orientation into the RVE. The centers of the disks were randomly generated, whereas their orientation was defined according to the distribution of the angles θ_x and θ_z, experimentally evaluated (Fig. 6), and reasonably approximated by a standard Gaussian distribution. For all simulations, a sequential generation of particles was performed imposing two conditions:

generated nanoparticles must not overlap each other within the domain;

parts of nanoparticles that intersect the outline, and so lie partly outside the RVE must be included in the RVE on the opposite side of the boundary.

If any of these conditions is violated, another particle is generated and the conditions are again checked. This instructions are cyclically repeated until the whole set of particles are generated.

This arrangement was used to obtain a RVE with geometrical periodicity that allows the implementation of the periodic boundary conditions. It can be demonstrated[47] that the application of these conditions allows to extrapolate the mechanical properties more accurately and with a minimum computational effort.

The geometrical constraints, introduced to face the basic assumptions of the algorithm and to optimize the geometrical design, affect the standard deviations of the particle orientation SD(θ) introduced as input parameters. To avoid this shortcoming, it was assumed the existence of a function $Y = Y(X)$ relating the standard deviations of the particle orientation in input $X = [\mathrm{SD}(\theta_{\mathrm{xin}}), \mathrm{SD}(\theta_{\mathrm{zin}})]$ with the value of the same parameters in output $Y = [\mathrm{SD}(\theta_{\mathrm{xout}}), \mathrm{SD}(\theta_{\mathrm{zout}})]$. In particular, linearizing this function around an appropriate point X_0 sufficiently close to desired values in output, it was possible to introduce the following expression:

$$Y = Y(X_0) + \nabla_{x_0} Y(X - X_0) \tag{15}$$

The gradient $\bigtriangledown_{x_0} Y$ was estimated by performing Monte Carlo random generation with variable X and then the values of SD(θ) in input were found to have the desired SD(θ) in output. With this procedure, it was possible to obtain, with a single iteration, values of standard deviation in output sufficiently close to experimental ones with an error rate of 5%.

The size of the RVE also represents a very critical parameter for obtaining accurate results, so the model sensitivity to the RVE dimensions is highlighted in a following paragraph.

The routine output of the previous calculation was a text file containing the command lines that can be read by the Ansys program for the generation of the geometric characteristics of the RVE elements (particle location file). The material characteristics of the composite phases were also introduced in this file in order to directly run the FEM calculations.

FEM Model

The portion of algorithm, written to generate the mesh and other FEM commands in Ansys environment (FEM routine), processes the data on the nanocomposite geometry, coming from the particle location file, allowing the construction of volumes and surfaces of the RVE. The silicate particles were assumed to be perfectly bonded to the polymer matrix and so, merged with the matrix during the realization of the FEM model.

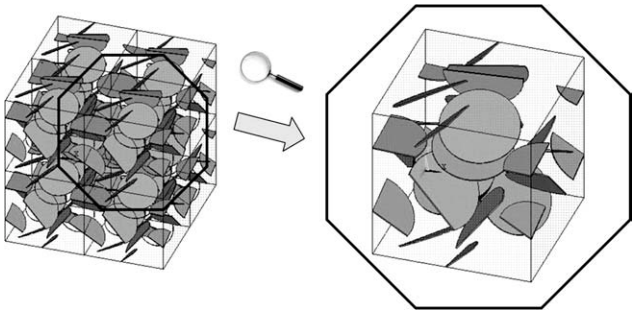

FIGURE 8 Geometric model built in Ansys environment.

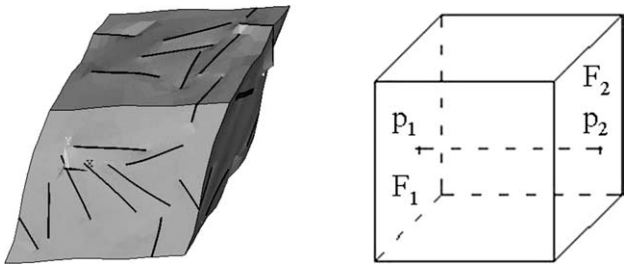

FIGURE 9 (a) Deformation due to the imposition of periodic boundary conditions (shear test); (b) points involved in the periodic boundary conditions.

At this point, the algorithm requires the definition of elements for the finite element discretization. The following element types were chosen:

- SOLID95 defined by 20 nodes each having three translational degrees of freedom.
- MESH200 that is a "mesh-only" element, not contributing to the solution.

This element is used, in this case, for drive the volume-meshing in 3D space. Its presence will not affect simulation results, but allows the creation of identical surface mesh on opposite sides of the RVE.

The convergence analysis of the results (in terms of mechanical properties) was realized through the variation of the average size of the nanoparticles mesh (under the assumptions of the H-method), and through the setting of the average size of the polymer matrix mesh to a value equal to 1/10 of the RVE dimension.[30] The nanoparticles mesh was varied from a maximum size equal to that of the matrix mesh, to a minimum value beyond which there were no significant changes in the results, because a stable asymptotic solution was reached. An identical analysis was performed on the same RVEs, at the same conditions, but dividing the average size of the matrix mesh in half. The mean percentage error obtained was equal to 0.006% compared with the results of the previous runs. For computational reasons (to shorten run times), the ratio between the average size of the polymer matrix mesh (set to a value equal to 1/10 of the size of RVE) and the average size of the nanoparticles mesh was set at the value of 2. Such a discretization overestimates the results of about 0.25% compared with the values obtained at the convergence. Such an error is inferior to the numerical approximations generally accepted.

Periodic Boundary Conditions

The model periodicity allows the imposition of periodic boundary conditions. Applying these conditions on the RVE, it is possible to simulate more accurately the real deformation phenomenon with respect to the displacement or stress conditions.[47] The conditions on the displacements, in this case, couple the displacements of each point located on opposite sides [Fig. 9(a)].

For example, if u_1, v_1, and w_1 are the displacements along x, y, and z, respectively, of the point P_1 on the face F_1, imposing only ε_x deformation, the following relations with the displacements u_2, v_2, and w_2 of the point P_2 (opposite to P_1 on the side F_2) have to hold [Fig. 9(b)]:

$$\begin{cases} u_2 = \varepsilon_x L + u_1 \\ v_2 = v_1 \\ w_2 = w_1 \end{cases} \tag{16}$$

In general, the imposed conditions involve each point on one side and the correspondent node on the opposite side. These conditions are expressed in the following synthetic matrix form:

$$u_2 - u_1 = \varepsilon(X_2 - X_1) \tag{17}$$

where X_i is the position vector of the point P_i, whereas u_i is the relative displacement vector.

In a finite element model it is sufficient to impose the conditions described above for each couple of nodes on each face. The logical sequence for the model consists of three steps: selection of a node on one side, selection of the node on the opposite side, and imposition of the three constraint equations along x, y, and z relating the displacements of these two nodes. This procedure is repeated until the whole set of nodes are coupled. The process is then repeated for the other two pairs of faces. Following this procedure, however, the displacement of some nodes already descended from the equations that couple the displacement of other nodes. To overcome this shortcoming, it is necessary to exclude some nodes of the RVE to have only constraint equations linearly independent.

There are a number of issues related to applying periodic boundary conditions with a FEM mesh[30] due to the difficulty in application of the coupling conditions. In this work, the FEM routine automatically creates identical surface mesh between opposite edges. Further, the node numbers to be coupled are individuated on the basis of their location. Finally, the opportune displacement equations, depending on the imposed average strain, are written. In Figure 10, a mesh example is presented.

Homogenized Modules

After the application of the boundary conditions, for each simulation, three static tensile tests and three static shear tests (with imposed average deformations) are automatically performed to have as output all stiffness matrix components of the nanocomposite film on the basis of some assumptions. Imposing the overall deformation $\langle\varepsilon\rangle = [0,...,\langle\varepsilon_i\rangle,...,0]$, and assuming small strains and elastic behavior of the material, it is possible to define the specific potential energy ϕ as (no sum over i):

$$\phi = \frac{1}{2}\overline{C_{ii}}\langle\varepsilon_i\rangle^2 \tag{18}$$

so the value of the component $\overline{C_{ii}}$ is given by:

$$\overline{C_{ii}} = 2\frac{\phi}{\langle\varepsilon_i\rangle^2} \tag{19}$$

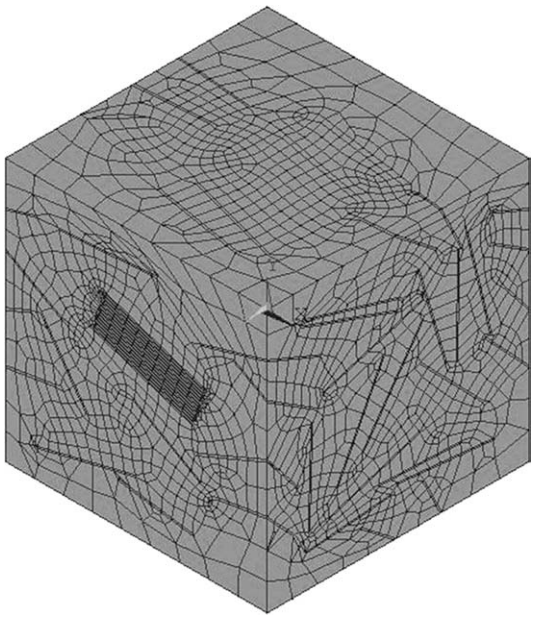

FIGURE 10 Mesh details of the model for 3D randomly oriented-particle distribution.

For each *i*th imposed deformation, the algorithm calculates, according to eq 19, the corresponding diagonal component of the matrix stiffness. The specific potential energy is calculated, as a result of the FEM analysis, using the following relation:

$$\phi = \frac{\sum_{\text{elem}} \phi_{\text{elem}} \text{vol}_{\text{elem}}}{\text{vol}_{\text{RVE}}} \tag{20}$$

and eq 19 becomes:

$$\overline{C_{ii}} = 2 \frac{\frac{\sum_{\text{elem}} \phi_{\text{elem}} \text{vol}_{\text{elem}}}{\text{vol}_{\text{RVE}}}}{\langle \varepsilon_i \rangle^2} \tag{21}$$

where ϕ_{elem} is the potential energy associated with a generic element due to the *i*th strain component, vol_{elem} is the element volume, and vol_{RVE} the volume of the RVE.

In addition, for each *i*th imposed deformation, the algorithm allows to calculate all the components of the corresponding *i*th column of the stiffness matrix, by using a different formulation.

From the elastic overall constitutive law, we can write:

$$\overline{\overline{C_{hi}}} = \frac{\langle \sigma_h \rangle}{\langle \varepsilon_i \rangle} \qquad \forall h, i = 1, \ldots, 6 \tag{22}$$

where the stress component $\langle \sigma_h \rangle$ is calculated in the FEM routine, using the following relation:

$$\langle \sigma_h \rangle = \frac{\sum_{\text{elem}} \sigma_{h\text{elem}} \text{vol}_{\text{elem}}}{\text{vol}_{\text{RVE}}} \tag{23}$$

where $\sigma_{h\text{elem}}$ is the *h*th stress component of the single element, due to the *i*th imposed deformation. In this way, with a single FEM run, characterized by six sequential imposed deformations, the algorithm allows to calculate the diagonal components of the stiffness matrix using an energetic method (that provides $\overline{C_{ii}}$ values), and all the components of the stiffness matrix with eq 22 (that provides $\overline{C_{ij}}$ values). The values of diagonal components, calculated with the two different criteria and resulting from simulations carried out for this article, were always equal for less than a maximum percentage error of 0.005%. This fact has confirmed the validity of eq 22 for the calculation of all components of the stiffness matrix.

Choice on the RVE Size: Isotropy Criterion

The RVE size influences the simulation computational effort and the possibility that the nanoparticle distribution can be distorted. In fact, in small RVEs the position of a nanoparticle may affect the position of the nanoparticles generated later. For this reason, a criterion for choosing the size of the RVE, which is directly related to the number of nanoparticles, is proposed. The target was to find the minimum size of RVE so that it could present isotropic structural characteristics, once the random generation of the parameters, relating each particle, was performed in the three-dimensional space (RVE).

The criterion is based on minimization of the following function:

$$|\Delta|^2 = \sum_{i,j=1}^{6} \left(C_{i,j} - C^I_{i,j}(\lambda, G) \right)^2 \tag{24}$$

where $C_{i,j}$ is the *i,j*th component of stiffness matrix extrapolated from the FEM calculation, $C^I_{i,j}$ is the *i,j*th component of the unknown isotropic stiffness matrix, λ and G represent the independent parameters that define the isotropic stiffness matrix (Lamè constants).The minimization of eq 24 leads to the determination of λ and G parameters that define the isotropic material closer (with regard to the mechanical behavior) to the material simulated by the Ansys calculation. Consequently, the algorithm calculates the norm of "difference tensor" $\Delta = C - C^I$ that gives information about the difference between the numerically calculated matrix and the ideal isotropic one. Then, the algorithm calculates a parameter δ, given by the ratio between the norm of the difference tensor Δ and the norm of the tensor C^I, which provides information on the isotropic degree in the composite depending on the size of the RVE (in terms of numbers of nanoparticles located). This criterion has shown that for RVE with a number of particles greater than 30, the value of the parameter δ tends to a small constant value (Fig. 11). This number of particles agrees with the data obtained from literature.[30]

Another criterion used for assessing the goodness of the model is the estimation of the components of the orthotropic stiffness matrix. For an ideal material, the only components different from zero are those of the first quadrant and those on the diagonal of the fourth quadrant. The stiffness coefficients, calculated by the FEM model, present maximum values of the components, homologous to those equal to zero in the ideal material, of an order of

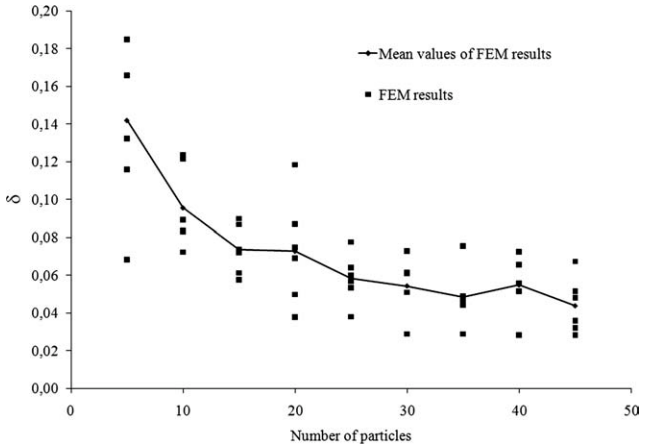

FIGURE 11 Plot of the parameter δ as a function of the number of particles.

magnitude (and in many case of two order) smaller than the calculated minimum values of the remaining components. Also in this case, 30 particles are sufficient to properly characterize the RVE.

FEM AND ANALYTICAL MODEL PREDICTIONS

In Figures 12 and 13, the comparisons between experimental and calculated results (obtained both by FEM and OMT models) are reported for the nanocomposite blown films. Each FEM calculated stiffness matrix was averaged over 5 runs, each corresponding to a different effective position of the silicate particles in the RVE, resulting from a random extraction. The small standard deviations resulting from the simulations have confirmed the reliability of the RVE model.

It can be observed that both the analytical and numerical models adequately describe the experimental mechanical behavior of the copolyamide-based nanocomposite films. Analyzing the histograms in Figures 12 and 13, it is also possible to highlight that the stiffness constants, predicted by OMT and FEM model, likely show the same behavior when compared with the experimental values. In particular, the OMT model slightly overestimates FEM results, in agreement with previous simulations reported in literature.[30]

As expected, the worst correspondence between experimental and predicted elastic modulus has been observed for the sample 3HADS35 along the transverse direction (E_z). This result can be due to the complex effects of drawing on the

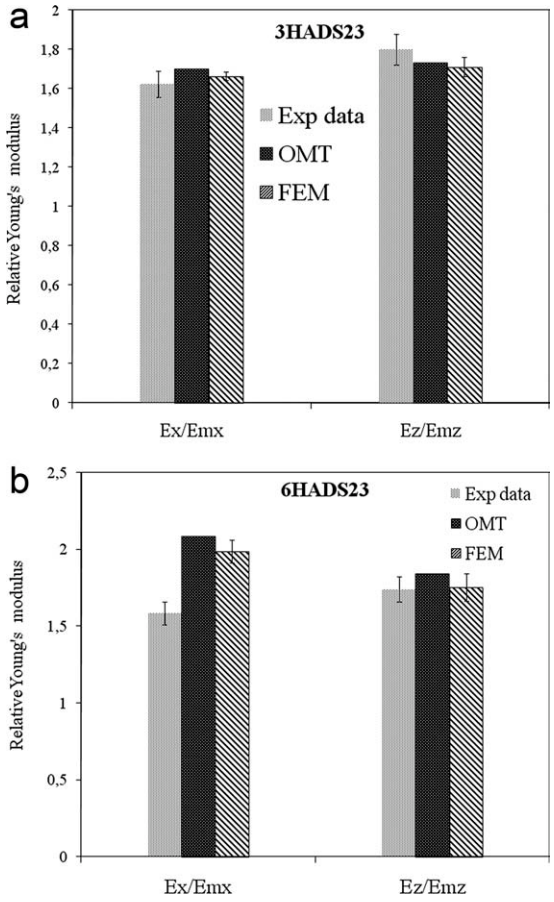

FIGURE 12 Comparison between experimental and calculated data: (a) 3HADS23 and (b) 6HADS23 nanocomposite blown films.

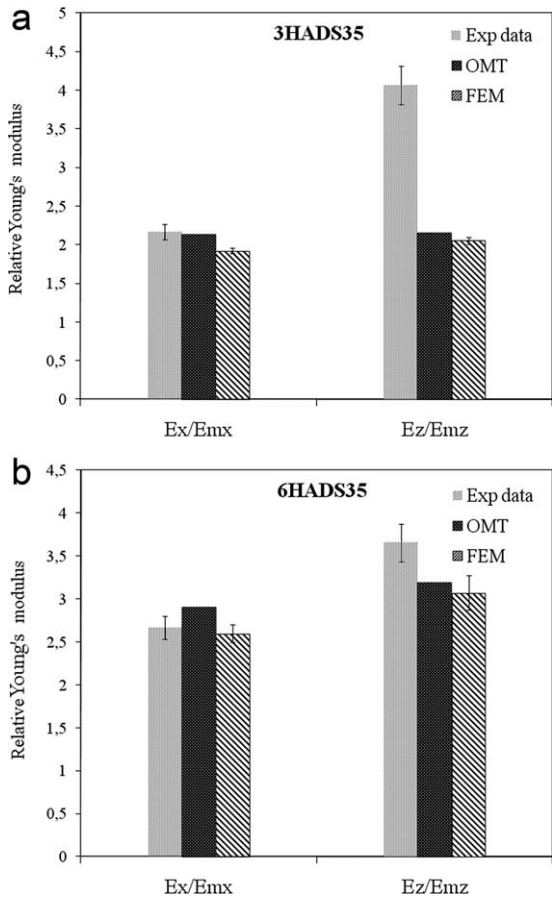

FIGURE 13 Comparison between experimental and calculated data: (a) 3HADS35 and (b) 6HADS35 nanocomposite blown films.

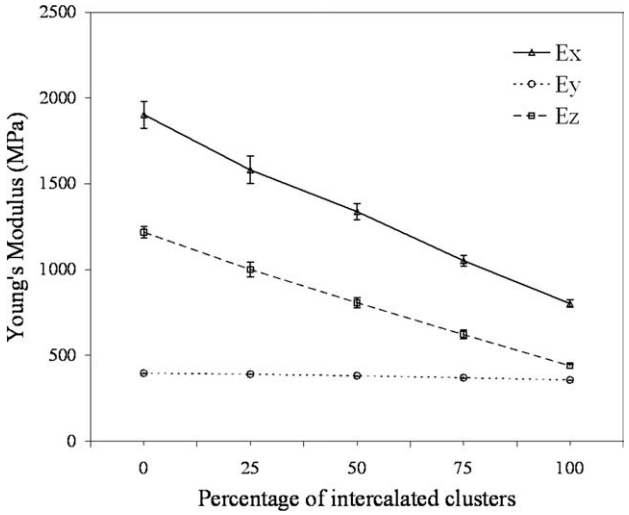

FIGURE 14 Stiffness constants of copolyamide-based nanocomposite blown films (6HADS35) at different exfoliation degrees.

crystalline structure and then on the mechanical properties of polyamide-based nanocomposite systems.[38,39]

Because the agreement between experimental data and FEM simulation results was very reasonable, it was possible to evaluate with confidence the effects of various model parameters on the stiffness constants of the nanocomposite blown films. This study was based on two reference systems (3HADS23 and 6HADS35 blown films) experimentally characterized. In particular, some morphological (exfoliation degree and number of platelets per stack) and geometrical (standard deviations of nanoclay orientation distribution) parameters, appearing in the numerical model, were independently varied keeping the others constant. The trends of the nanocomposite stiffness constants, resulting from FEM sensitivity analysis, are reported in Figures 14–16.

It was found that the fraction of completely exfoliated clay particles is the most effective parameter in enhancing stiffness of the hybrids. A key issue in forming polymer nanocomposites is, in fact, achieving high levels of silicate exfoliation, as extensively reported in literature.[1–3] However, in the commonly occurring case, the clay particles are not fully dispersed and a mixed intercalated/exfoliated morphology is obtained. In Figure 15, the effect of the average number of platelets per stack (n) on the composite modulus is reported. It can be observed a considerable reduction of the elastic constants (E_x and E_z) by increasing the value of n from one (completely exfoliated system) to only two or three clay layers per stack. For this analysis, the intercalated clusters were treated in a very simple way, considering clay layers, having equal diameter, stacked directly on top of one another. Moreover, the gallery volume was experimentally evaluated to be comparable with the volume occupied by the silicate platelets and, as consequence, the nanocomposite modules drop abruptly with increasing n. A simple explanation of these modules reduction is given in literature,[15] reporting that an increase of the number of platelets per stack inherently reduces the equivalent particle's aspect ratio.

The orientation of the dispersed phase also affects the composite modules. In particular, deviations from unidirectional reinforcement can result in sizeable reductions in nanocomposite stiffness and this effect may be amplified depending on the filler shape. As evidenced in Figure 16, the stiffness constants E_x and E_z assume their maximum values when the silicate platelets are oriented in the same plane of the film (SD(θ_x) and SD(θ_z) tend to zero), whereas the nanocomposite system consistently behaves as an isotropic material by increasing the standard deviations of θ_x and θ_z angles. The orientation of the filler, respect to the applied load, will dictate the mechanism of stress transfer. When the filler is misaligned or in the extreme case perpendicular to the applied load, the stress at the interface varies from a shear mode

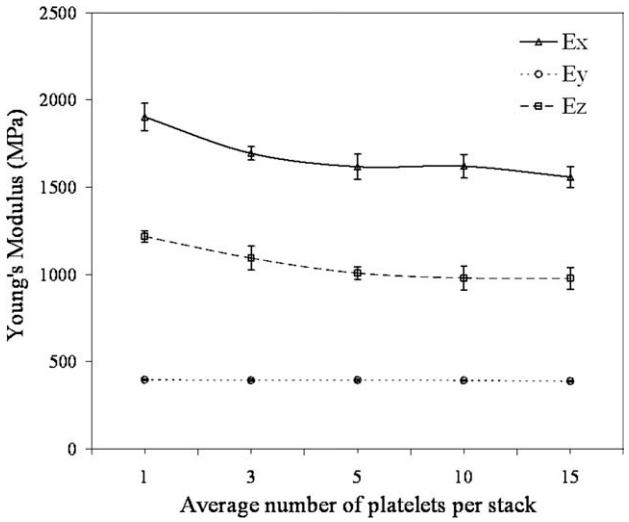

FIGURE 15 Stiffness constants of copolyamide-based nanocomposite blown films (6HADS35) as a function of the number of silicate platelets per stack.

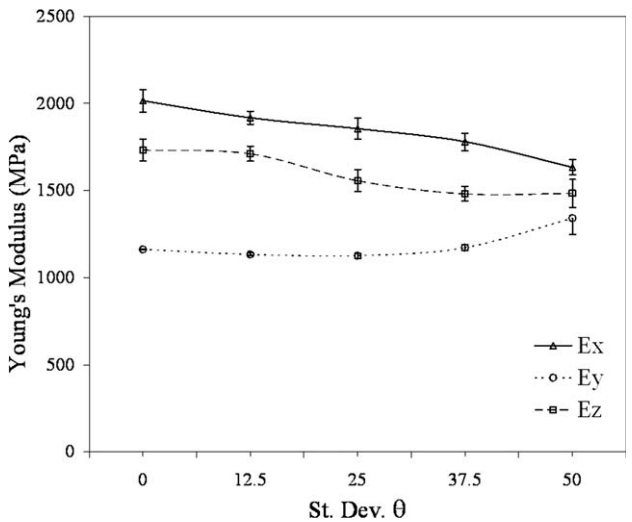

FIGURE 16 Stiffness constants of copolyamide-based nanocomposite blown films (3HADS23) at different standard deviations of θ_x and θ_z angles.

into a tensile mode. This fact generates a higher concentration of stress in the matrix and less tension in the filler particle, similar to what happens at the edge of a platelet.

CONCLUSIONS

This work was focused on the modeling of mechanical behavior of polyamide based nanocomposite films whose tensile properties were related to the morphological modifications, in terms of silicate nanostructure and polymer orientation, due to the biaxial deformation imposed during the film blowing process.

To properly take into account the very complex nanostructure observed in the blown films, a three-dimensional finite element model has been realized using an original algorithm that generates the clay particles position on the basis of the measured silicate platelets orientation. Furthermore, the polymer matrix was considered to be elastically orthotropic, as a consequence of the process-induced macromolecular orientation during film blowing. Periodic boundary conditions and an original RVE sizing method were also used to minimize the dimensions of the RVE that gives acceptable scatter and to avoid overlong computational times.

Experimental elastic constants of the polyamide nanocomposite films were also compared with analytical predictions based on the Mori-Tanaka approach that was properly modified to take into account the mechanical orthotropic characteristics of the polymer matrix upon drawing.

Comparison of simulation results with experimental data has confirmed the reliability of both the analytical and numerical models used in this study. However, it is worthy to point out the bigger potentialities of a FEM-based micromechanical approach compared with an analytical model. In particular, a numerical simulation method allows modeling the behavior at the nanoparticle-matrix interface that is fundamental to properly analyze the mechanisms of fracture for these systems. A main feature of a FEM model is also the capability to plot the tensional distributions in order to have a three-dimensional map of stresses' transmission throughout the different phases of the composite, allowing to optimize the model, once the sensitive parameters were identified. Furthermore, the FEM method allows to investigate many other properties, often fundamental for practical applications of these materials, such as thermal and permeability properties and to model dynamic phenomena characterized by both material and geometrical nonlinearity.

REFERENCES AND NOTES

1 Pinnavaia, T. J. In Polymer-Layered Silicate Nanocomposites; Beall, G. W., Ed.; Wiley: New York, **2001.**

2 Alexandre, M.; Dubois, P. *Mater. Sci. Eng.* **2000,** *28*, 1–63.

3 LeBaron, P. C.; Wang, Z.; Pinnavaia, T. J. *Appl. Clay Sci.* **1999,** *15*, 11–29.

4 Shah, R. K.; Paul, D. R. *Polymer* **2004,** *45*, 2991–3000.

5 Paul, D. R.; Robeson, L. M. *Polymer* **2008,** *49*, 3187–3204.

6 Incarnato, L.; Scarfato, P.; Scatteia, L.; Acierno, D. *Polymer* **2004,** *45*, 3487–3496.

7 Russo, G. M.; Simon, G. P.; Incarnato, L. *Macromolecules* **2006,** *39*, 3855–3864.

8 Weon, J. I.; Sue, H. J. *Polymer* **2005,** *46*, 6325–6334.

9 Borse, N. K.; Kamal, M. R. *Polym. Eng. Sci.* **2006,** *46*, 1094–1103.

10 Masenelli-Varlot, K.; Reynaud, E.; Vigier, G.; Varlet, J. *J. Polym. Sci. Part B: Polym. Phys.* **2002,** *40*, 272–283.

11 VanderHart, D. L.; Asano, A.; Gilman, J. W. *Chem. Mater.* **2001,** *13*, 3796–3809.

12 Anastasiadis, S. H.; Karatasos, K.; Vlachos, G.; Manias, E.; Giannelis, E. P. *Phys. Rev. Lett.* **2000,** *84*, 915–918.

13 Zax, D. B.; Yang, D. K.; Santos, R. A.; Hegemann, H.; Giannelis, E. P.; Manias, E. *J. Chem. Phys.* **2000,** *112*, 2945–2951.

14 Incarnato, L.; Scarfato, P.; Russo, G. M.; Di Maio, L.; Iannelli, P.; Acierno, D. *Polymer* **2003,** *44*, 4625–4634.

15 Fornes, T. D.; Paul, D. R. *Polymer* **2003,** *44*, 4993–5013.

16 Kinlock, A. J.; Taylor, A. C. *J. Mater. Sci.* **2006,** *41*, 3271–3297.

17 Wang, J.; Pyrz, R. *Compos. Sci. Technol.* **2004,** *64*, 925–934.

18 Wang, J.; Pyrz, R. *Compos. Sci. Technol.* **2004,** *64*, 935–944.

19 Brune, D. A.; Bicerano, J. U. *Polymer* **2002,** *43*, 369–387.

20 Valavala, P. K.; Odegard, G. M. *Rev. Adv. Mater. Sci.* **2005,** *9*, 34–44.

21 Van Es, M.; Xiqiao, F.; van Turnhout, J.; Van der Giessen, E. In Comparing Polymer–Clay Nanocomposites with Conventional Composites Using Composite Modelling; Al-Malaika, S.; Golovoy, A. W., Eds.; Blackwell Science: CA Malden, **2001; Chapter 21.**

22 Hui, C. Y.; Shia, D. *Polym. Eng. Sci.* **1998,** *38*, 774–782.

23 Shia, D.; Hui, C. Y.; Burnside, S. D.; Giannelis, E. P. *Polym. Compos.* **1998,** *19*, 608–617.

24 Figiel, Ł.; Buckley, C. P. *Comput. Mater. Sci.* **2009,** *44*, 1332–1343.

25 Sheng, N.; Boyce, M. C.; Parks, D. M.; Rutledge, G. C.; Abes, J. I.; Cohen, R. E. *Polymer* **2004,** *45*, 487–506.

26 Scocchi, G.; Posocco, P.; Danani, A.; Pricl, S.; Fermeglia, M. *Fluid Phase Equilib.* **2007,** *261*, 366–374.

27 Luo, J-J.; Daniel, I. M. *Compos. Sci. Technol.* **2003,** *63*, 1607–1616.

28 Garofalo, E.; Russo, G. M.; Di Maio, L.; Incarnato, L. *e-Polymers* **2009.**

29 Zhu, L.; Narh, K. A. *J. Polym. Sci. Part B: Polym. Phys.* **2004,** *42*, 2391–2406.

30 Hbaieb, K.; Wang, Q. X.; Chia, Y. H. J.; Cotterell, B. *Polymer* **2007,** *48*, 901–909.

31 Li, Y.; Waas, A. M.; Arruda, E. M. *J. Mech. Phys. Solids* **2011,** *59*, 43–63.

32 Li, Y.; Waas, A. M.; Arruda, E. M. *Int. J. Solids Struct.* **2011,** *48*, 1044–1053.

33 Liu, H.; Brinson, L. C. *Trans. ASME* **2006,** *73*, 758–768.

34 Liu, H.; Brinson, L. C. *Compos. Sci. Technol.* **2008,** *68*, 1502–1512.

35 Garofalo, E.; Russo, G. M.; Scarfato, P.; Incarnato, L. *J. Polym. Sci. Part B: Polym. Phys.* **2009,** *47*, 981–993.

36 Park, S.-Y.; Cho, Y.-H.; Vaia, R. A. *Macromolecules* **2005,** *38*, 1729–1735.

37 Vermogen, A.; Masanelli-Varlot, K.; Duchet-Rumeau, J.; Boucard, S.; Prele, P. *Macromolecules* **2005,** *38*, 9661–9669.

38 Russo, G. M.; Garofalo, E.; Montesano, S.; Incarnato, L. In Proceedings of PPS 24TH Conference, Salerno, Italy, June 15–19, **2008; pp 1–4.**

39 Garofalo, E.; Russo, M. G.; Incarnato, L.; Di Maio, L. In Proceedings of 17th International Conference on Composite Materials, Edinburgh, United Kingdom, July 27–31, **2009; pp 1–10.**

40 Ward, I. M.; Hadley, D. W. In An Introduction to the Mechanical. Properties of Solid Polymer; Wiley: New York, **1993.**

41 Ward, I. M. In Structure and Properties of Oriented Polymers; Chapman & Hall: London SE1 8HN, UK, **1997.**

42 Ponte Castañeda, P.; Willis, J. R. *J. Mech. Phys. Solids* **1995,** *43*, 1919–1951.

43 Benveniste, Y. *Mech. Mater.* **1987,** *6*, 147–157.

44 Benveniste, Y.; Dvorak, G. J.; Chen, T. *J. Mech. Phys. Solids* **1991,** *39*, 927–946.

45 Schjødt-Thomsen, J.; Pyrz, R. *Mech. Mater.* **2001,** *33*, 531–544.

46 Kinoshita, N.; Mura, T. *Phys. Status Solidi* **1971,** *5*, 759–768.

47 Hori, M.; Nemat-Nasser, S. *Mech. Mater.* **1999,** *31*, 667–682.